RSC Advances

PAPER

View Article Online
View Journal | View Issue

Check for updates

Cite this: *RSC Adv.*, 2019, **9**, 30925

Layer dependence of the photoelectrochemical performance of a WSe_2 photocathode characterized using *in situ* microscale measurements

Yu Zhang,* Jingwei Xiao, Xi Xie, Huanjun Chen and Shaozhi Deng

Received 13th August 2019
Accepted 23rd September 2019

DOI: 10.1039/c9ra06297a

rsc.li/rsc-advances

Transition-metal dichalcogenide (TMD) materials are good candidates for photoelectrochemical (PEC) electrode materials because of their distinctive optoelectronic properties and catalytic activities. Monolayer WSe_2 is a p-type semiconductor with a direct bandgap that makes it a suitable PEC cathode material. In the present work, *in situ* PEC characterization of a single sheet device was carried out at the microscale to explore its performance. The PEC characteristics were found to be strongly related to the number of WSe_2 layers. Monolayer WSe_2 exhibited a dominant large current density and incident photo-to-current efficiency (IPCE) compared with those of multilayer WSe_2. Its PEC performance decreased with increasing number of layers. The photocurrent mapping results also revealed that the basal-plane sites and the edge sites on a monolayer WSe_2 sheet contributed equally to its catalytic activity, which is not consistent with traditional catalyst theory. The underlying mechanism is discussed.

Introduction

Hydrogen, which as a high gravimetric energy density (~120 MJ kg^{-1}), is an ideal clean, sustainable, and highly efficient energy carrier that can potentially solve the worldwide energy crisis. Intensive research has been conducted to realize the efficient production of hydrogen.[1,2] Photoelectrochemical (PEC) water splitting, where solar energy is used to drive the thermodynamically uphill electrolysis reaction is a promising approach to generating hydrogen.[3,4] As a key component of PEC cells, the photoelectrode materials determine the light-harvesting efficiency and strongly influence the solar-to-hydrogen conversion efficiency. Various photoanode materials have been investigated in this application, including TiO_2,[5–7] ZnO,[8,9] WO_3,[10,11] $CuWO_4$ (ref. 12) and Fe_2O_3.[13,14] Previously explored photocathode materials include silicon,[15] InGaP[16] and Cu_2O.[17] Unfortunately, the large bandgap or unsuitable band-edge position seriously limits the water-splitting efficiency of PECs fabricated using these materials. Therefore, further development of stable and tunable PEC cathode materials is necessary.

A good PEC cathode material fulfills three basic requirements: (1) it exhibits p-type semiconductivity; (2) it exhibits a bandgap larger than 1.23 eV to drive the water electrolysis reaction[18] (given the overpotentials of water electrolysis, a bandgap greater than 1.5 eV is preferred); and (3) its band-edge potential is greater than the water redox potential. Otherwise, an external bias is needed to drive the reaction. Few materials satisfy these requirements. The emergence of transition-metal dichalcogenides (TMDs) with tunable optoelectronic properties has introduced new opportunities to satisfy the aforementioned requirements.[18–20] Among the TMDs, WSe_2 is a good candidate PEC cathode material. As a bulk crystal, WSe_2 is an indirect-bandgap semiconductor with a bandgap of 1.2 eV,[21,22] which is not ideal for PEC water splitting. Thus, the PEC efficiency of bulk crystalline WSe_2 is poor. Abruna and Bard reported the PEC characteristics of polycrystalline p-type WSe_2 films as photocathodes in 1982.[23] Recently, Lewis *et al.* used *in situ* measurements to investigate the PEC character of WSe_2 crystals at their terraces.[24] However, the properties of WSe_2 change when it is prepared as a monolayer sheet instead of as a bulk crystalline material. As a monolayer atomic-thin sheet, WSe_2 is a direct-bandgap semiconductor whose bandgap extends to 1.6 eV, which is suitable for PEC.[25] Thus, Yu *et al.* developed a space-confined self-assembled thin-film deposition method to fabricate large-area WSe_2 flake thin films and decorated them with Pt to improve their PEC performance.[26] However, the relationship between the thickness of WSe_2 and its PEC characteristics remains unclear. The intrinsic performance of monolayer WSe_2 and its dependency on the layer number are interesting topics that warrant further study.

Thin films are a standard style of PEC cathode material. However, the material properties of thin films are not unique.

State Key Laboratory of Optoelectronic Materials and Technologies, Guangdong Province Key Laboratory of Display Material and Technology, School of Electronics and Information Technology, Sun Yat-sen University, Guangzhou 510275, China. E-mail: stszhyu@mail.sysu.edu.cn

Numerous factors, including grain boundaries, orientation, stacking, thickness, and conductivity, contribute to the performance of thin films,[27,28] and distinguishing which factor dominates the performance is difficult. Measuring a single-sheet PEC cathode is preferable for characterizing its intrinsic performance.

In the present work, we introduce an *in situ* method to measure the PEC intrinsic characteristics of single-sheet WSe_2. The layer-dependent PEC characteristic of WSe_2 are investigated. Compared with multilayer WSe_2, the single-layer WSe_2 exhibits superior current density and superior incident photo-to-current efficiency (IPCE). The PEC performance decreases with increasing number of layers. We also found out that the basal-plane atoms contribute equally to the edge sites in a single-sheet WSe_2, which is not consistent with traditional catalyst theory.

Experimental

Microscale PEC device fabrication

A microscale PEC device was fabricated on a silicon substrate with a 300 nm-thick layer of SiO_2 using microfabrication techniques. An improved mechanical exfoliation method was adopted to achieve a single WSe_2 sheet with dimensions of several tens of micrometers. First, WSe_2 thin sheets were exfoliated onto Scotch tape. Second, the Scotch tape was adhered to and then stripped from a photoresist layer. Some of the WSe_2 flakes adhered to the photoresist. Then one of the WSe_2 flakes on the photoresist were locally transferred to the target Au electrode by using a dry transfer method.[29,30] Third, the photoresist film was removed with acetone. The WSe_2 flakes on the Au electrode act as a photocathode. Another Au electrode was deposited as the counter anodic electrode 1.5 millimeters away. A schematic of the *in situ* system is shown in Fig. 1.

To reduce the dark current and leakage current of the on-chip device and exclude some other effect, such as laser induced gold plasmon, the device surface was covered with a thin layer of polymethyl methacrylate (PMMA). Electron-beam lithography was used to expose the reaction windows of the WSe_2 sheet cathode and the Au anode electrode to air. Al wires were bonded onto two Au electrode stripe pads to connect the PEC device to the external circuit. Finally, a droplet of 0.5 M H_2SO_4 solution was dripped onto the PEC device as an electrolyte. The coverage area of the droplet was approximately 2×10^{-3} mm^2.

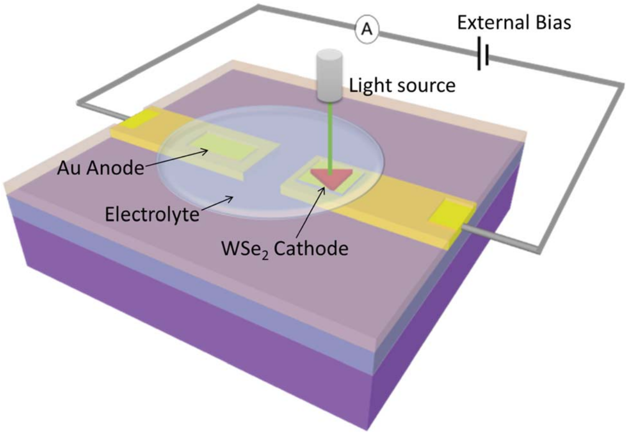

Fig. 1 Schematic of the *in situ* PEC measurement setup.

In situ PEC measurement

Unlike the general thin-film PEC measurements performed at the centimeter scale, a precise setup is needed to measure the PEC characteristics of a single sheet at the micrometer scale. We constructed an *in situ* PEC measurement system to precisely investigate the intrinsic characteristics of single sheets and elucidate their underlying chemical mechanism at the microscopic scale. This system enables the detection of a weak signal from a small sample and has a microscopic spatial resolution that provides quantitative data and 2D mapping analysis. The system was mainly reconstructed on a Raman platform (RENISHAW). The *in situ* system consists four parts: a light source, a sample holder, a mobile platform and an electric circuit. The system schematic is shown in Fig. 1. A laser was used as an input light. The minimum spot size of the laser was 1 μm, and the laser power was adjustable. The focus laser illuminating the local site of a WSe_2 sheet acted as incident solar energy. The advantage of using a focused light spot is (1) enable the light to irradiate precisely on the location of WSe_2 sheet; (2) avoid the light irradiate on the other place. Under irradiation, the Au anode has the plasmon effect to generate a plasmon-induced hot electron current[31,32] which could interfere with the signal from the cathode. Thus, the WSe_2 cathode and Au anode should be placed away from each other and the spot size of light should be as small as possible.

A 3D mobile platform monitored by a stepper motor controlled the sample's position. The step-to-step precision was 0.3 μm. The illumination position and area on the sample could thus be accurately controlled. Using the line scan function, the photocurrent and its position information was recorded accordingly, thus the 2D current mapping was achieved. It also enabled the *in situ* photocurrent and the photoluminescence spectrum to be measured and mapping simultaneously.

An external bias was applied to the circuit to promote the reaction. A source measure unit (Agilent B2902) was used to apply a bias voltage and collect the photocurrent at the picoampere level. In a typical linear sweep voltammetry data acquisition, the voltage applied to the working electrode was swept from 0 to 1 V at a scan rate of 100 mV s^{-1}. When the light was on, the PEC current was detected by the ammeter.

The electrolyte was 0.5 mol L^{-1} Na_2SO_4 solution. Due to the sample area is in mm scale, the electrolyte was dropped on the sample as a droplet with a syringe. It is noted that the small volume of electrolyte fast evaporated during test and it may cause the increase of concentration of electrolyte solution. To solve this problem, a small transparent PDMS box was designed to cover on the sample surface and store the electrolyte solution. In this way most of the electrolyte keep shielded from the air to reduce the evaporate rate and the solution can stayed stable in half an hour which is long enough for testing.

Material characterization

The Raman and photoluminescence (PL) spectra of WSe_2 were recorded with a RENISHAW Raman spectrometer equipped with a 532 nm laser (incident power of 70 μW). The thickness of the WSe_2 was measured with an atomic force microscope (NT-MDT NTEGRA Spectra). The morphology of the WSe_2 flake was observed with an OLYMPUS BX53 optical microscope. The absorbance spectra of the microscale WSe_2 film was measured using an optical time-domain spectroscopy which was modified to focus the incident light to micrometer scale.

Results

Raman and PL spectroscopy were used to confirm the quality and layer number of the WSe_2 nanoflakes. In definition, the monolayer WSe_2 has 1 layer; the fewlayer WSe_2 has 2–10 layers; the multilayer WSe_2 has large than 10 layers. Fig. 2(a) shows the optical microscope images of a monolayer and multilayers of WSe_2 flakes transferred onto Au electrodes. The layer number of the WSe_2 sheet was determined from its color. The Au electrode was yellow, and the deep-yellow monolayer WSe_2 was clearly observed to cover the Au electrode; the orange and wine-red sheets were fewlayer and multilayer WSe_2, respectively. The atomic force microscopy (AFM) measurements further confirmed the thickness of the WSe_2 sheet (Fig. 2(b)). The AFM step height of the WSe_2 monolayer on the Au electrode was typically measured as 1.0 nm, consistent with previously published results.[25,33]

The Raman spectra of the monolayer, fewlayer, and multilayer WSe_2 are plotted in Fig. 2(c). All of the spectra show two strong peaks at approximately 250 cm^{-1}, corresponding to the $E_{2g}{}^1$ and A_{1g} modes of WSe_2.[34] The Raman spectrum of monolayer WSe_2 is plotted as a red curve. No Raman $B_{2g}{}^1$ mode was observed at 310 cm^{-1}, confirming that the sheet was a monolayer.[35,36] The Raman spectra of the fewlayer and multilayer WSe_2 nanosheets are plotted as blue, green, and black lines. Small peaks are observed at approximately 310 cm^{-1}, corresponding to the $B_{2g}{}^1$ resonance mode of WSe_2, which indicates additional interlayer interaction, thereby demonstrating fewlayer nanosheet characteristics.

Fig. 2(d) shows the PL spectra of the monolayer, fewlayer, and multilayer WSe_2 nanosheets. The PL spectrum of the monolayer WSe_2 shows a strong single peak at approximately 1.63 eV; its full-width at half-maximum (FWHM) was 0.09 eV (red curve). The strong emission and a symmetric single PL peak at 1.63 eV reflect the direct-bandgap nature of monolayer

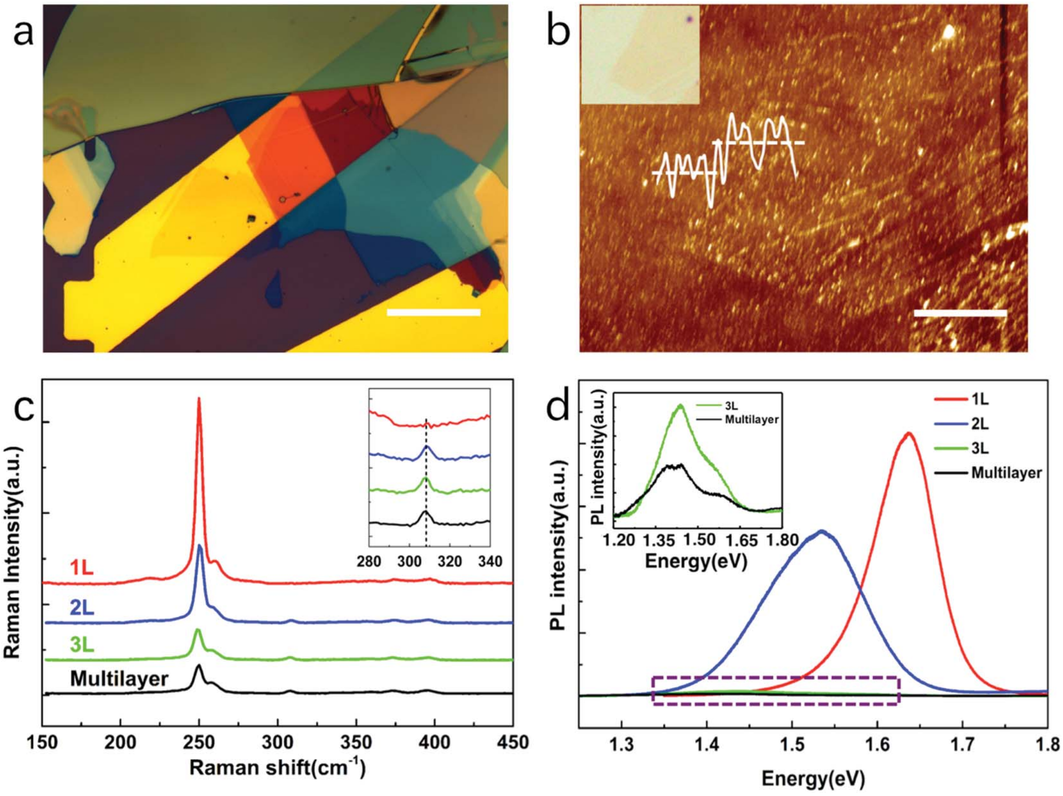

Fig. 2 Characterizations of WSe_2 sheets. (a) Optical images of a WSe_2 sheets covering the Au electrode. The number of layers was identified by the color: the monolayer, fewlayer, and multilayer films are deep-yellow, orange, and dark-green, respectively. Scale bar is 50 μm. (b) AFM thickness scans of the monolayer WSe_2 film and the line-scan profile on its edge. The inset is the optical image of the same measured area. (c) Raman spectra of monolayer (red, 1L), bilayer (blue, 2L), trilayer (green, 3L), and multilayer (black) WSe_2. The inset shows the bulk $B_{2g}{}^1$ Raman mode of fewlayer WSe_2 at approximately 310 cm^{-1}; the spectrum of monolayer WSe_2 does not shows the $B_{2g}{}^1$ bulk Raman mode. (d) PL spectra of monolayer (red, 1L), bilayer (blue, 2L), trilayer (green, 3L), and multilayer (black) WSe_2. The inset is an enlarged view of the PL spectra of trilayer and multilayer WSe_2.

WSe_2.[37,38] The PL spectrum of the bilayer WSe_2 showed a much wider PL peak in 1.53 eV (blue curve)[34,39] which consists of two peaks 1.51 eV and 1.63 eV. The peak in 1.51 eV represents the indirect transition band and 1.63 eV represents the main direct transition band. Thus, the bilayer WSe_2 has both peaks and small peak shift comparing to monolayer. The PL spectra of trilayer and multilayer WSe_2 showed a very weak peak in 1.4 eV and its FWHM is as large as 0.2 eV which consist of a series of peaks (inset of Fig. 3(d)). It is a typical spectrum of bulk WSe_2. The weak intensity and the large peak shift reflect that the multilayer WSe_2 has an indirect-bandgap nature.

The PEC characteristics of WSe_2 sheets with different layer numbers were measured. Monolayer, fewlayer (2–4 layers), and multilayer (more than 5 layers) WSe_2 sheets, which exhibit deep-yellow, orange, and dark-green colors, were selected for measurement, as shown in Fig. 2(a). First, the sample was coated with a thin layer of PMMA. Then the PMMA on the selected area was removed using electron-beam lithography to make the selected area exposing to the light and the electrolyte. During the measurement, a white-light spot was focused on the selected local area of a WSe_2 sheet mounted on the platform of an optical microscope, and the photocurrent was detected with an ammeter. The light spot was 0.1 mm in diameter. The current–voltage curve shown in Fig. 3(a) demonstrates that the monolayer WSe_2 sheet exhibited a much larger photocurrent than the other two sheets. The maximum current density reached 20 μA cm^{-2} when an external bias of 1 V was applied. By contrast, the current density was 5 and 0.2 μA cm^{-2} for the fewlayer and multilayer WSe_2 sheets, respectively. The onset voltage for monolayer WSe_2 was 0.2 V, whereas it was 0.6 V and 0.8 V for the fewlayer and multilayer WSe_2, respectively. The photocurrent response in Fig. 3(b) also demonstrates better performance of the monolayer WSe_2 sheet. The WSe_2 sheet demonstrated good photocurrent stability. During the ~3 h measurement, the photocurrent remained stable, with no obvious degradation.

The IPCE of the WSe_2 sheets was calculated; the results are shown in Fig. 3(d). The IPCE of the monolayer WSe_2 sheet was approximately 2% in the range 600–800 nm and was even higher (2–4%) at 450–600 nm, showing excellent light-harvesting efficiency in the visible wavelength range. The IPCE of the fewlayer and multilayer WSe_2 sheets was 0.8% and 0.4%, which were much smaller than that of the monolayer WSe_2. Given that the light absorbance of monolayer WSe_2 is only ~10% (Fig. 3(c)), the photon-to-current conversion efficiency of monolayer WSe_2 is very high. This high photon-to-current conversion efficiency is attributed to the monolayer WSe_2 having a direct bandgap suitable for the visible-light spectrum, which enables it to harvest more visible-spectrum photons and facilitates the generation of photon-generated carriers.[40] Thus, more electron–

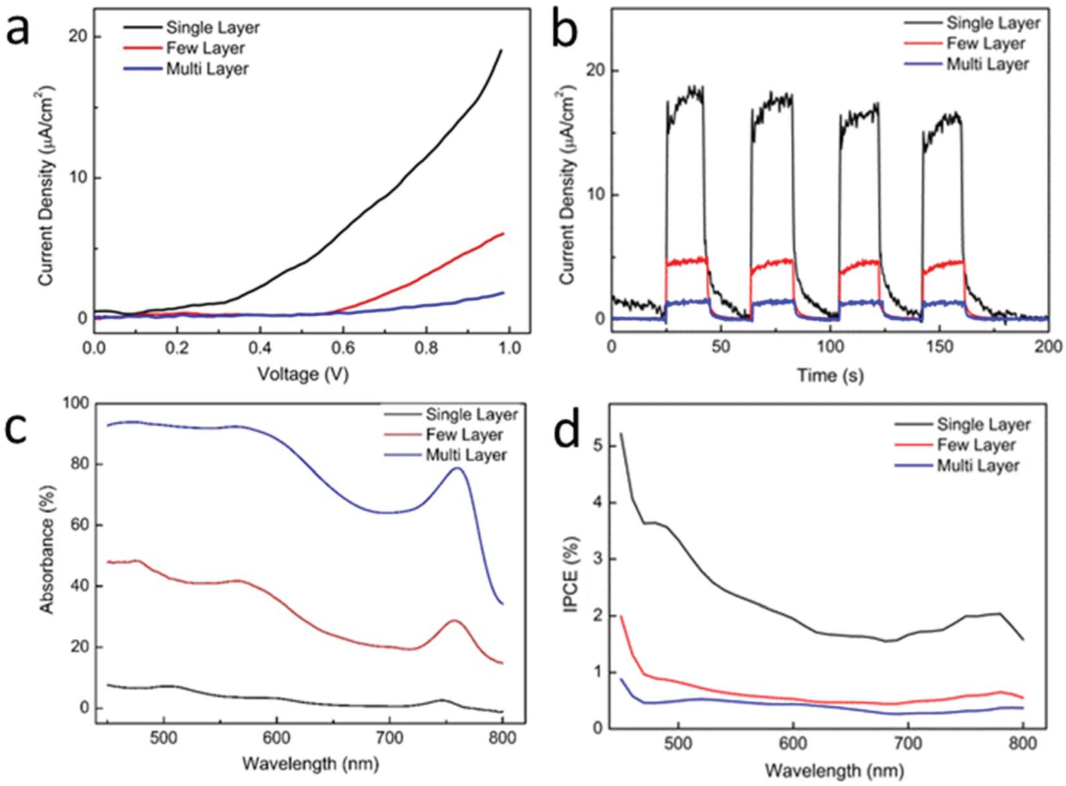

Fig. 3 PEC characteristics of a single WSe_2 sheet with different layer numbers. The monolayer, fewlayer, and multilayer WSe_2 sheets are represented in black, red, and blue. (a) PEC current *vs.* voltage curve under focused white-light illumination. (b) Photocurrent response curve. The cycle period is 50 s and the light-on time is 25 s. (c) Light absorption curves of WSe_2 sheets. (d) The incident-photon-to-current (IPCE) spectrum of WSe_2 sheets.

hole pairs are formed and participate in the redox reaction. Therefore, the PEC current density and the IPCE both increased. By contrast, multilayer WSe_2, which has an indirect bandgap, requires additional energy to overcome the transverse momentum and thus cannot directly generate photon-generated carriers. The efficiency of photons generating electron–hole pairs is low, adversely affecting the PEC characteristics in a multilayer WSe_2 sheet. On the basis of these results, the PEC characteristics of the 2D WSe_2 sheets are strongly dependent on their layer number. The monolayer WSe_2 sheet is an optimal choice for the PEC cathode. The ability to fabricate a monolayer WSe_2 cathode would be an important factor in improving its performance as a PEC electrode material.

A photocurrent mapping measurement was carried out to investigate the surface catalyst activity of a monolayer WSe_2 sheet. As shown in Fig. 4(a), a monolayer WSe_2 sheet was transferred onto an Au electrode. The circuit setup was the same as that in the previous measurement. The light source was a 532 nm laser with a spot size of 1 μm. The laser power was 70 μW, and the scanning step was set to 0.3 μm which should be smaller than the spot size. The laser then scanned the WSe_2 sheet surface and the photocurrent was measured. Meanwhile, the PL intensity signal was simultaneously recorded. In this measurement, the photocurrent distribution on the 2D surface was clearly demonstrated.

Two regions of monolayer WSe_2 were measured (see Fig. 4(a), marked with white-dashed rectangles A and B). The PL intensity mapping of regions A and B (Fig. 4(b) and (d)) reveals that both regions of the WSe_2 sheet are monolayers with uniform crystallinity. Some dark spots observed on the mapping image indicate regions of weaker PL intensity, possibly representing defects. The shape of the PL map matches well with the morphology of the WSe_2 sheet. The corresponding 2D color mapping images of the photocurrent are shown in Fig. 4(c) and (e). The color changed from blue to red, indicating a change in the photocurrent from low to high. The results clearly show that the photocurrent is generated from the WSe_2 sheet, but not the bare Au electrode. The shape of the photocurrent maps also matched well with the PL intensity maps and optical images which means the photocurrent mapping was correlated with the shape of WSe_2. The regions covered by the monolayer WSe_2 display strong signals. There are several hot spots observed as yellow and red regions in the photocurrent mapping indicating that the photocurrent higher than average level was achieved there. These spots were likely defects such as vacancies or impurities which was normally introduced in the mechanical exfoliation and dry transfer process. It is known that the defects create localized states within the bandgap. These sub-gap states help to harvest the light below the bandgap energy and increase the incident light harvesting efficiency. In addition, the defects also are the catalyst active sites which increase the attraction of ions in the solution and increase the rates of reaction. In turn it resulted in higher PEC efficiency.[41]

To our surprise, the photocurrent on the edge of the WSe_2 sheet did not show a strong response. The response current at the edge was slightly lower than that in the basal plane and gradually decreased to the background level. Both regions showed the same results, meaning that the monolayer WSe_2

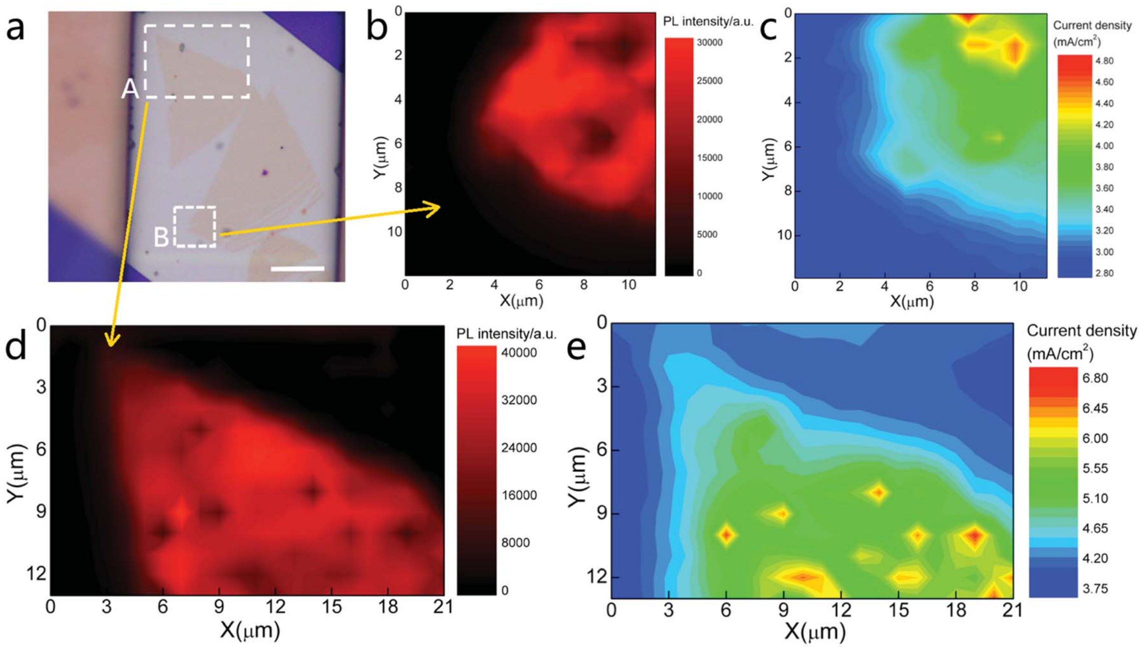

Fig. 4 (a) Optical image of measured WSe_2. The scanning areas are marked with white-dashed rectangular regions A and B. Scale bar: 10 μm. (b) and (d) Photoluminescence intensity mappings of regions A and B. The main peak 1.63 eV was selected. The incident laser was 532 nm and the power was 70 μW. (c) and (e) Photocurrent maps of regions A and B. The illumination time for each spot was 3 s. The external applied bias was 0.9 V. The region was scanned line by line. Scanning step in region A: 1 μm per step in both the *X* and *Y* directions. Scanning distance in region B: 0.7 μm per step in both the *X* and *Y* directions.

does not exhibit higher photocatalytic activity at its edge than on its basal plane. On the basis of traditional theory, catalytic activity at the edge of a bulk material is much stronger than that in the basal plane.[42,43] The catalyst activity in the basal plane is sufficiently small to be ignored. Therefore, edges are deliberately introduced when designing a material to increase its catalytic activity.[44–46] However, this phenomenon is not observed on a monolayer sheet (2D material).

We speculate that, in the case of a 2D material with a single-atomic-layer, the inside and outside of the material do not substantially differ. For a 2D material, only a surface exists, not an interior. No interior atoms exist to restrict the activity of atoms at the basal-plane surface. The basal plane and the edge exhibit the same activity toward the solution. Therefore, the reaction rate should be the same across the whole surface. This model introduces the possibility of greatly increasing the PEC efficiency because the whole surface of a 2D material is active toward the redox reaction. Monolayer sheets have a very large surface with a catalytic activity much greater than that of a bulk material,[47] greatly benefiting their PEC performance.

Conclusion

In this work, we showed that monolayer WSe_2 is an excellent PEC cathode material. Using an *in situ* PEC characterization system, a microscale PEC device with single-sheet WSe_2 as the cathode was precisely investigated. The WSe_2 sheet without any catalyst showed a remarkable photocurrent of 20 $\mu A\ cm^{-2}$. The IPCE was as high as 2–4% in the visible spectrum. The PEC characteristics were strongly related to the layer number of WSe_2. Specifically, the monolayer WSe_2 had a direct bandgap and a suitable bandgap in the visible spectrum and therefore exhibited excellent optoelectronic properties. The photocurrent mapping of the WSe_2 sheet revealed a surprising phenomenon in that the active sites on the basal plane and those on the edge of single-sheet WSe_2 contributed equally to the catalytic activity, which is not consistent with traditional catalyst theory. We speculated that the special structure of the 2D material consisting of a single-atomic-layer surface liberates the catalyst activity on the basal plane. These initial results demonstrate that using TMD layered materials as PEC electrodes is a promising approach to water-splitting. The optoelectronic properties of a single-sheet TMD in the visible-wavelength portion of the spectrum and its high catalyst activity on its whole surface would benefit its PEC performance and its water-splitting performance.

Conflicts of interest

The authors declared that they have no conflicts of interest to this work.

Acknowledgements

This work was supported by the National Natural Science Foundation of China (grant no. 51672314, 61874142, and 51290271), the Guangdong Natural Science Foundation (grant no. 2016A030313359), the Science and Technology Program of Guangzhou (grant no. 201707010224), the Science and Technology Department of Guangdong Province, the Fundamental Research Funds for the Central Universities.

References

1 I. Roger, M. A. Shipman and M. D. Symes, *Nat. Rev. Chem.*, 2017, **1**, 0003.
2 J. K. Stolarczyk, S. Bhattacharyya, L. Polavarapu and J. Feldmann, *ACS Catal.*, 2018, **8**, 3602–3635.
3 R. H. Coridan, A. C. Nielander, S. A. Francis, M. T. McDowell, V. Dix, S. M. Chatman and N. S. Lewis, *Energy Environ. Sci.*, 2015, **8**, 2886–2901.
4 M. G. Walter, E. L. Warren, J. R. McKone, S. W. Boettcher, Q. Mi, E. A. Santori and N. S. Lewis, *Chem. Rev.*, 2010, **110**, 6446–6473.
5 I. S. Cho, C. H. Lee, Y. Feng, M. Logar, P. M. Rao, L. Cai, D. R. Kim, R. Sinclair and X. Zheng, *Nat. Commun.*, 2013, **4**, 1723.
6 G. Wang, X. Xiao, W. Li, Z. Lin, Z. Zhao, C. Chen, C. Wang, Y. Li, X. Huang, L. Miao, C. Jiang, Y. Huang and X. Duan, *Nano Lett.*, 2015, **15**, 4692–4698.
7 K. Jeong, P. R. Deshmukh, J. Park, Y. Sohn and W. G. Shin, *ACS Sustainable Chem. Eng.*, 2018, **6**, 6518–6526.
8 B. S. Wang, R. Y. Li, Z. Y. Zhang, X. Wang, X. L. Wu, G. A. Cheng and R. T. Zheng, *Catal. Today*, 2019, **321**, 100–106.
9 Y. Lan, Z. Liu, Z. Guo, X. Li, L. Zhao, L. Zhan and M. Zhang, *Dalton Trans.*, 2018, **47**, 12181–12187.
10 G. Wang, Y. Ling, H. Wang, X. Yang, C. Wang, J. Z. Zhang and Y. Li, *Energy Environ. Sci.*, 2012, **5**, 6180–6187.
11 Y. Li, Z. Liu, J. Zhang, Z. Guo, Y. Xin and L. Zhao, *J. Alloys Compd.*, 2019, **790**, 493–501.
12 Z. Liu, Q. Song, M. Zhou, Z. Guo, J. Kang and H. Yan, *Chem. Eng. J.*, 2019, **374**, 554–563.
13 J. Wang, J. L. Waters, P. Kung, S. M. Kim, J. T. Kelly, L. E. McNamara, N. I. Hammer, B. C. Schmehl, R. H. Pemberton, A. Gupta and S. Pan, *ACS Appl. Mater. Interfaces*, 2017, **9**, 381–390.
14 D. Chen and Z. Liu, *ChemSusChem*, 2018, **11**, 3438–3448.
15 L. A. King, T. R. Hellstern, J. Park, R. Sinclair and T. F. Jaramillo, *ACS Appl. Mater. Interfaces*, 2017, **9**, 36792–36798.
16 H. Wang and J. A. Turner, *Energy Environ. Sci.*, 2013, **6**, 1802–1805.
17 D. Chen, Z. Liu, Z. Guo, W. Yan and Y. Xin, *J. Mater. Chem. A*, 2018, **6**, 20393–20401.
18 A. Kudo and Y. Miseki, *Chem. Soc. Rev.*, 2009, **38**, 253–278.
19 U. Gupta and C. N. R. Rao, *Nano Energy*, 2017, **41**, 49–65.
20 X. Chia, A. Ambrosi, Z. Sofer, J. Luxa and M. Pumera, *ACS Nano*, 2015, **9**, 5164–5179.
21 D. Gerchman and A. K. Alves, *J. Colloid Interface Sci.*, 2016, **468**, 247–252.
22 Q. H. Wang, K. Kalantar-Zadeh, A. Kis, J. N. Coleman and M. S. Strano, *Nat. Nanotechnol.*, 2012, **7**, 699–712.

23 H. D. Abruna and A. J. Bard, *J. Electrochem. Soc.*, 1982, **129**, 673–675.

24 J. M. Velazquez, J. John, D. V. Esposito, A. Pieterick, R. Pala, G. Sun, X. Zhou, Z. Huang, S. Ardo, M. P. Soriaga, B. S. Brunschwig and N. S. Lewis, *Energy Environ. Sci.*, 2016, **9**, 164–175.

25 H. Zhou, C. Wang, J. C. Shaw, R. Cheng, Y. Chen, X. Huang and X. Duan, *Nano Lett.*, 2015, **15**, 709–713.

26 X. Yu, M. S. Prévot, N. Guijarro and K. Sivula, *Nat. Commun.*, 2015, **6**(7596), 1–8.

27 J. Xie, H. Zhang, S. Li, R. Wang, X. Sun, M. Zhou and Y. Xie, *Adv. Mater.*, 2013, **25**, 5807–5813.

28 Y. Yin, J. Han, Y. Zhang, X. Zhang, P. Xu, Q. Yuan and P. Zhang, *J. Am. Chem. Soc.*, 2016, **138**, 7965–7972.

29 Y. Liu, N. O. Weiss, X. Duan, H. C. Cheng, Y. Huang and X. Duan, *Nat. Rev. Mater.*, 2016, **1**, 16042.

30 J. Xiao, Y. Zhang, H. Chen, N. Xu and S. Deng, *Nano-Micro Lett.*, 2018, **10**(60), 1–9.

31 J. Lee, S. Mubeen, X. Ji, G. D. Stucky and M. Moskovits, *Nano Lett.*, 2012, **12**, 5014–5019.

32 S. Mukherjee, L. Zhou, A. M. Goodman, N. Large, C. Ayala-Orozco, Y. Zhang and N. J. Halas, *J. Am. Chem. Soc.*, 2013, **136**, 64–67.

33 H. Li, G. Lu, Y. Wang, Z. Yin, C. Cong, Q. He and H. Zhang, *Small*, 2013, **9**, 1974–1981.

34 E. del Corro, H. Terrones, A. Elias, C. Fantini, S. Feng, M. A. Nguyen and M. A. Pimenta, *ACS Nano*, 2014, **8**, 9629–9635.

35 P. Tonndorf, R. Schmidt, P. Böttger, X. Zhang, J. Börner, A. Liebig and S. M. de Vasconcellos, *Opt. Express*, 2013, **21**, 4908–4916.

36 W. Zhao, Z. Ghorannevis, L. Chu, M. Toh, C. Kloc, P. H. Tan and G. Eda, *ACS Nano*, 2012, **7**, 791–797.

37 B. Liu, M. Fathi, L. Chen, A. Abbas, Y. Ma and C. Zhou, *ACS Nano*, 2015, **9**, 6119–6127.

38 J. K. Huang, J. Pu, C. L. Hsu, M. H. Chiu, Z. Y. Juang, Y. H. Chang and L. Li, *ACS Nano*, 2013, **8**, 923–930.

39 Z. Li, S. Yang, R. Dhall, E. Kosmowska, H. Shi, I. Chatzakis and S. B. Cronin, *ACS Nano*, 2016, **10**, 6836–6842.

40 N. R. Pradhan, J. Ludwig, Z. Lu, D. Rhodes, M. M. Bishop, K. Thirunavukkuarasu and L. Balicas, *ACS Appl. Mater. Interfaces*, 2015, **7**, 12080–12088.

41 H. Li, C. Tsai, A. L. Koh, L. Cai, A. W. Contryman, A. H. Fragapane, J. Zhao, H. S. Han, H. C. Manoharan, F. Abild-Pedersen, J. K. Nørskov and X. Zheng, *Nat. Mater.*, 2016, **15**, 48–53.

42 T. Zambelli, J. Wintterlin, J. Trost and G. Ertl, *Science*, 1996, **273**, 1688.

43 T. F. Jaramillo, K. P. Jørgensen, J. Bonde, J. H. Nielsen, S. Horch and I. Chorkendorff, *Science*, 2007, **317**, 100–102.

44 J. Kibsgaard, Z. Chen, B. N. Reinecke and T. F. Jaramillo, *Nat. Mater.*, 2012, **11**, 963.

45 S. Kanda, T. Akita, M. Fujishima and H. Tada, *J. Colloid Interface Sci.*, 2011, **354**, 607–610.

46 H. Wang, C. Tsai, D. Kong, K. Chan, F. Abild-Pedersen, J. K. Nørskov and Y. Cui, *Nano Res.*, 2015, **8**, 566–575.

47 B. Cho, M. G. Hahm, M. Choi, J. Yoon, A. R. Kim, Y. J. Lee and Y. Jeong, *Sci. Rep.*, 2015, **5**, 8052.